Appl. Phys. B 70, 579–586 (2000) / Digital Object Identifier (DOI) 10.1007/s003400000213

Applied Physics B
Lasers
and Optics

Evanescent wave scattering by aggregates of clusters – application to optical near-field microscopy

M. Quinten

I. Physikalisches Institut A, RWTH Aachen, 52056 Aachen, Germany
(E-mail: quinten@physik.rwth-aachen.de)

Received: 27 August 1999/Revised version: 8 November 1999/Published online: 1 March 2000 –

Abstract. Extended Mie-theory is used to investigate scattering and extinction of evanescent waves by aggregates of clusters. In an application to apertureless near-field optical microscopy involving total internal reflection at the surface substrate–air, the variation of the scattered power is calculated when a silicon particle is scanned across single clusters or aggregates of clusters in the evanescent field. Metallic, dielectric, and semiconducting particles are taken into consideration, and the dependence on sizes, materials, and the wavelength is discussed.

PACS: 78.20.Bh; 78.66.Vs; 42.25.Fx

Evanescent waves are a central topic in scanning near-field optical microscopy (SNOM), as such waves carry the information that yields optical resolution below the Abbe limit. Experimental setups used for SNOM employ evanescent waves generated either by a conventional tapered SNOM fiber probe acting as light source or by total internal reflection at a dielectric interface. The latter is used, for example, in photon scanning tunneling microscopy (PSTM) [1, 2] where a probe tip is moved into the evanescent field above the sample surface and partly converts it into propagating waves, which can be detected in the far field. Another example is the recent development of a near-field optical microscope, employing scattering of an evanescent wave at a nanometer-sized silicon tip of a standard cantilever interacting with the sample [3, 4], which has yielded spatial resolution in the 1-nm range, i.e. far beyond the diffraction limit of conventional optical microscopes. In this setup the scattering of the evanescent wave has been detected interferometrically by means of a Nomarski microscope. This approach is unique in that it combines scanning force microscopy, an apertureless variant of SNOM, and confocal far-field microscopy.

The wide potential applications of such a scattering microscopy and spectroscopy, especially in biology, medicine, materials science, and information technology have motivated us to consider scattering and extinction of evanescent waves by aggregates of small particles or clusters and to calculate *x*-*y*-*z* scans of a near-field probe across a surface with single clusters or cluster aggregates.

The basic formulae for scattering of evanescent waves by a single spherical particle were already given by Chew et al. [5] in 1979. Their theory was slightly corrected by Liu et al. [6]. Recently, we extended these results on total cross sections for evanescent-wave excitation and discussed their dependence on wavelength, angle of incidence, and cluster sizes for homogeneous [7] and coated particles [8]. By means of numerical field calculations employing the multiple multipole (MMP) method [9] we have also studied the effects when the cluster is on the surface where the evanescent wave is generated by total internal reflection (TIR). The latter may be summarized as follows: particle resonances are generally broadened, damped, and slightly redshifted by multiple scattering at the interface.

As in scanning optical near-field microscopy the electromagnetic interaction among the tip and particles on a substrate or a glass prism becomes important [10–14], we extended the theory of electromagnetic coupling among spherical particles on evanescent fields. Particularly apertureless near-field optical microscopy, where TIR is employed, is considered in detail in the following. In a first approach to the problem of calculating the power scattered from the tip–sample region, we model the probe tip by a spherical particle of radius a_0 and assume single spheres of radius a_1 or aggregates of identical clusters of radius a_1 as the sample. In order to understand the basic properties of evanescent-wave scattering by such a multi-particle complex, we further assume that we can neglect multiple scattering effects involving the surface. It can be expected that the influence of the surface in this scattering problem is similar to that in case of a single particle on a substrate.

Optical effects associated with aggregates of identical nm-sized clusters are well known for silver and gold clusters [15–21]. They are determined by the splitting of the surface plasmon resonance of the isolated particle into new modes due to the electromagnetic coupling among the particles, yielding changes in the absorption and scattering spectrum as well as in the differential cross section. For other nm-sized particles the spectral contributions of these modes

could not be resolved, but the electromagnetic coupling resulted in deviations from Rayleigh scattering [22]. For larger particles for which geometrical resonances can be resolved, the splitting into new geometrical resonances is also observable [22]. In the present case, even optical constants of the tip material and the cluster material must not be equal. However, this is not a restriction and was already studied in detail for plane-wave excitation in a recent work [23].

The paper is organized as follows. In Sect. 1 we briefly repeat the theory of evanescent-wave scattering by a single cluster and the theory of scattering by an aggregate of clusters. We present and discuss numerical results for *x*-*y*-*z* scans of a tip–particle over a surface with single clusters in Sect. 2 and for particle aggregates of various topology in Sect. 3. Finally, in Sect. 4 a summary of the results is given.

1 Theory

In the following section, we briefly repeat the expressions for the optical cross sections of a single spherical particle with evanescent-wave excitation obtained in [7]. According to the definition employed in this reference, the cross sections for extinction and scattering of an evanescent wave by a spherical particle with diameter $2a$ are for *s*-polarised incident light:

$$\sigma_{\mathrm{ext}}^{s}(1) = \frac{2\pi}{k^2}\frac{1}{No}\mathrm{Re}\sum_{n=1}^{\infty}(2n+1)\,(a_n\Pi_n + b_n T_n)\ , \tag{1a}$$

$$\sigma_{\mathrm{sca}}^{s}(1) = \frac{2\pi}{k^2}\frac{1}{No}\sum_{n=1}^{\infty}(2n+1)\left(|a_n|^2\Pi_n + |b_n|^2 T_n\right)\ , \tag{1b}$$

for *p*-polarised incident light:

$$\sigma_{\mathrm{ext}}^{p}(1) = \frac{2\pi}{k^2}\frac{1}{No}\mathrm{Re}\sum_{n=1}^{\infty}(2n+1)\,(a_n T_n + b_n\Pi_n)\ , \tag{1c}$$

$$\sigma_{\mathrm{sca}}^{p}(1) = \frac{2\pi}{k^2}\frac{1}{No}\sum_{n=1}^{\infty}(2n+1)\left(|a_n|^2 T_n + |b_n|^2\Pi_n\right)\ , \tag{1d}$$

with the definitions

$$\Pi_n(\theta_k) = \frac{2}{n(n+1)}\sum_{m=-n}^{n}\frac{(n-m)!}{(n+m)!}\left|m\frac{P_{nm}(\cos\theta_k)}{\sin\theta_k}\right|^2\ , \tag{2a}$$

$$T_n(\theta_k) = \frac{2}{n(n+1)}\sum_{m=-n}^{n}\frac{(n-m)!}{(n+m)!}\left|\frac{\mathrm{d}P_{nm}(\cos\theta_k)}{\mathrm{d}\theta_k}\right|^2\ , \tag{2b}$$

and the coefficients a_n and b_n being the scattering coefficients of the TM-modes and TE-modes of the spherical particle, respectively. θ_k is the angle of incidence in the reference frame of the particle. It depends on the angle of incidence θ_i at the interface glass substrate–air via Snell's law

$$\cos\theta_k = \frac{n_{\mathrm{P}}}{n_{\mathrm{M}}}\sin\theta_i\ , \tag{3}$$

with n_{P} being the index of refraction of the glass subtrate and n_{M} being the index of refraction of the surrounding medium (here: air).

Formulae (1a–d) are also valid for coated spherical particles with an arbitrary number of layers, or hollow spheres. Only the expressions for the coefficients a_n, b_n differ in these cases. For an incident plane wave at the particle site, i.e. $\cos\theta_k \le 1$ and $\theta_i \le \theta_{\mathrm{c}}$, θ_{c} being the critical angle of total internal reflection, $T_n = \Pi_n = 1$ for all multipolar orders n. In this case the cross sections are, of course, equal for *s*- and *p*-polarisation and (1) are the well-known results from standard Mie-theory (see for example [24]). For an incident evanescent wave ($\theta_i > \theta_{\mathrm{c}}$) it follows from Snell's law that $\cos\theta_k > 1$. Then, the functions T_n, Π_n increase with the order n and with the angle of incidence, and can attain very large values [7].

The normalisation factor No is equal to one for plane waves, but assumes a different value for evanescent waves. If the cross section is normalized to the total incident power, No is given by

$$No = \frac{n_{\mathrm{P}}}{n_{\mathrm{M}}}\sin\theta_i\left(1+\sum_{m=1}^{\infty}\frac{(\kappa a)^{2m}}{m!(m+1)!}\right)\ , \tag{4}$$

with

$$\kappa = \frac{2\pi}{\lambda}\left(n_{\mathrm{P}}^2\sin\theta_i - n_{\mathrm{M}}^2\right)^{1/2}\ . \tag{5}$$

The polarisation dependence of the cross sections is due to the fact that *p*- and *s*-polarised evanescent waves are not related to each other by a simple rotation: for *p*-polarised waves the electric field is rotating in the plane of incidence, due to the complex phase shift associated with total internal reflection, whereas for *s*-polarised waves it is oscillating perpendicular to it.

The extinction and scattering cross sections for an aggregate with N spherical particles are [25]:

$$\sigma_{\mathrm{ext}}(N) = \frac{2\pi}{k^2}\sum_{i=1}^{N}\sum_{n=1}^{\infty}\sum_{m=-n}^{n}\mathrm{Re}\{\alpha_{nm}(i)+\beta_{nm}(i)\}\ , \tag{6}$$

$$\begin{aligned}\sigma_{\mathrm{sca}}(N) = {}& \frac{2\pi}{k^2}\sum_{i=1}^{N}\sum_{n=1}^{\infty}\sum_{m=-n}^{n}|\alpha_{nm}(i)|^2+|\beta_{nm}(i)|^2 \\ & + \frac{2\pi}{k^2}\sum_{i=1}^{N}\sum_{n=1}^{\infty}\sum_{m=-n}^{n}\mathrm{Re}\left\{\alpha_{nm}^{*}(i)\left(1-\frac{\alpha_{nm}(i)}{a_n(i)}\right)\right. \\ & \left. + \beta_{nm}^{*}(i)\left(1-\frac{\beta_{nm}(i)}{b_n(i)}\right)\right\}\ .\end{aligned} \tag{7}$$

$\alpha_{nm}(i)$ and $\beta_{nm}(i)$ are the expansion coefficients of the scattered wave of particle i, which can be resolved from solution of linear sets of equations following from Maxwell's boundary conditions at the surface of each particle i. The electromagnetic coupling becomes negligible for center-to-center distances $d_{ij} \ge 5(a_i + a_j)$ [25]. Then, the cross sections of the aggregate reduce to the sum over cross sections of N isolated spheres.

Extinction and scattering of light by an arbitrary N-sphere aggregate depend on the sizes of the primary particles, the size and topology of the aggregate, the particle materials

and the polarization and propagation direction of the incident wave. The simplest aggregate is a pair of clusters. In this case two principal excitation modes of the aggregate are obtained: the *longitudinal mode*, when the electric field vector of the incident wave is along with the axis of the pair, and *transverse mode* with the electric field being perpendicular to this axis. In the general case of arbitrary incidence of the plane wave both modes contribute to a certain amount to the absorption and scattering by the pair. For illustration, Fig. 1 depicts the optical extinction efficiency spectra of single, isolated clusters of Ag and Si with $2a = 40$ nm in air and of pairs of clusters Ag−Ag and Ag−Si with identical sizes for the longitudinal and the transverse mode. The extinction cross sections of the pair and the isolated particles are computed at wavelengths between 300 nm and 600 nm. For convenience, in all spectra the cross sections are normalized to the geometrical cross section, i.e. πa^2 for the single particles and $2\pi a^2$ for the pair of clusters, obtaining the dimensionless extinction efficiency Q_{ext}. As the particles are small compared to the wavelength of incident light, it is assumed that maximum the quadrupolar mode efficiently contributes to the spectrum.

The Ag-cluster exhibits a surface plasmon resonance peaked at wavelength $\lambda = 372$ nm. This is the resonance of the TM-dipole mode a_1 that mainly contributes to the spectrum. The corresponding TE-dipole mode b_1 does not exhibit a resonance and is two orders of magnitude smaller than a_1. Higher multipolar contributions are negligible. The spectrum of the Si-cluster is also dominated by the dipolar contribution, but does not exhibit a corresponding resonance. The coupling among two adjacent silver particles obviously leads to a splitting of the cluster plasmon resonance into the longitudinal mode and transverse mode. For the longitudinal mode the corresponding peak is redshifted (peak position $\lambda = 424$ nm), and for the transverse mode a blueshift (peak position $\lambda = 365$ nm) is obtained with respect to the peak position of the single-cluster plasmon resonance.

The cluster plasmon resonance of the silver particle gets affected also in the case of coupling with a silicon cluster. Then the splitting into longitudinal and transverse mode is, however, smaller than in the previous case of two silver clusters (peak positions: transverse mode $\lambda = 372$ nm, longitudinal mode $\lambda = 387$ nm). Moreover, the efficiencies are decreased by about a factor of two. In both cases, however, the efficiency of the longitudinal mode is larger than the efficiency of the transverse mode in the whole spectral region.

Formulae (6) and (7) are valid for plane-wave excitation and must be extended appropriately to take into account evanescent-wave excitation. This was done, but will not be shown in detail. Instead, we present exemplary results for the extinction efficiency spectrum of a pair of silver clusters with $2a = 40$ nm on the glass substrate in Fig. 2. The spectra are compared with spectra obtained for a plane wave with grazing incidence at the substrate. For the plane wave the electric field vector is always perpendicular to the pair axis. Then, the spectra for *s*- and *p*-polarisation must coincide, showing the spectrum of the transverse mode with retardation of the incident wave at the site of the second particle. The peak position is $\lambda = 366$ nm, close to the peak position of the unretarded transverse mode. For the evanescent wave, the spectrum in *s*-polarisation is rather similar to that for the plane wave and

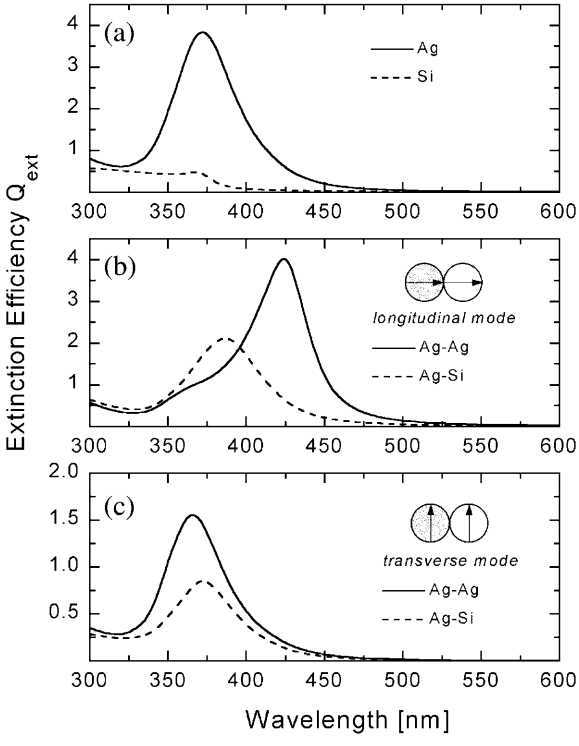

Fig. 1a–c. Extinction efficiency spectra of isolated Ag and Si clusters (**a**), the longitudinal mode of pairs Ag−Ag and Ag−Si (**b**), and the transverse mode of pairs Ag−Ag and Ag−Si (**c**). The *vertical line* represents the peak position of the single silver cluster plasmon resonance

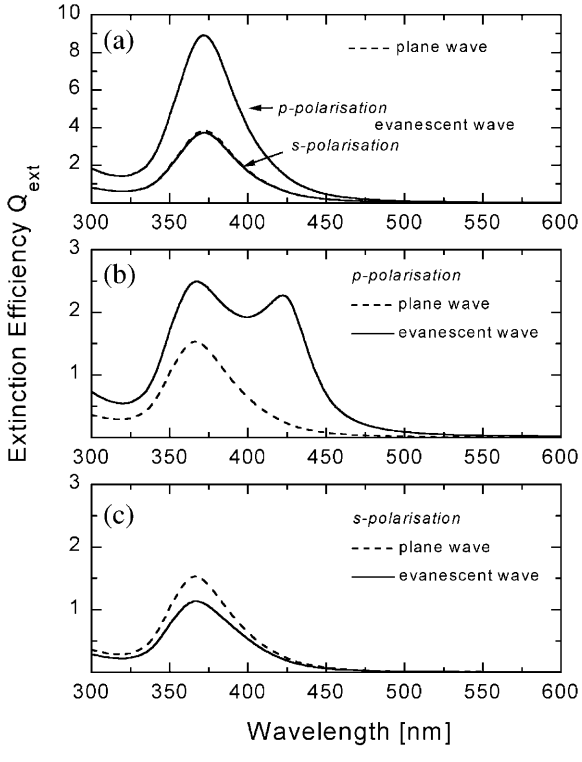

Fig. 2a–c. Extinction efficiency spectra of an isolated Ag for plane-wave excitation and *p*-polarised and *s*-polarised evanescent excitation (**a**), the pair Ag−Ag for *p*-polarized plane-wave excitation in grazing incidence and *p*-polarised evanescent wave excitation (**b**), and the pair Ag−Ag for *s*-polarized plane-wave excitation in grazing incidence and *p*-polarised evanescent wave excitation (**c**)

is peaked at the same wavelength. In contrast, the spectrum in *p*-polarisation shows a resonance at $\lambda = 422$ nm that can be assigned to the longitudinal mode, in addition to the transverse mode that is peaked at $\lambda = 367$ nm. This is due to the fact that for *p*-polarised evanescent waves the electric field is rotating in the plane of incidence, due to the complex phase shift associated with total internal reflection. Then, it can almost always be decomposed in a component parallel and perpendicular to the pair axis. The efficiency in *p*-polarisation is at least by a factor of two larger than in *s*-polarisation.

2 Results and discussion for single clusters on a substrate

In the following section exemplary results from *x*-*y*-*z* scans of a probe over a surface with single clusters will be presented. They are representative for more than 70 calculations. Figure 3 is a sketch of the geometry in this scattering problem. In all calculations it is assumed that the evanescent wave is generated by total internal reflection at the interface glass–air with an angle of incidence of $\theta_i = 60°$. The corresponding index of refraction of the glass prism was assumed to amount to $n_P = 1.5$ at all wavelengths under consideration. In all cases, the scan range is 400×400 nm in the *x*-*y* plane, and the calculation has been performed for 200×200 positions of the scanning probe particle. The silicon particle is scanned across the silver sphere at different heights *z* of its center relative to the glass substrate, also allowing contact of both particles when the probe is at $x = 0$, $y = 0$.

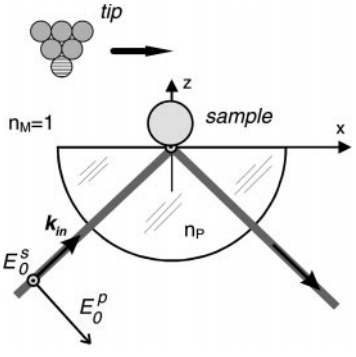

Fig. 3. Sketch of the scattering geometry for the scan of a Si-cluster across a surface with a single spherical particle in the center of the reference frame

Figure 4 displays the scattered intensity obtained in a scan of a silicon particle with $2a_0 = 20$ nm across a surface with a single Ag-cluster with $2a_1 = 40$ nm at the height $z = 50$ nm (touching spheres at $x = 0$, $y = 0$) for both polarisations. The scan was performed at wavelength $\lambda = 514$ nm.

The difference between *s*- and *p*-polarisation is evident from the figure. In *p*-polarisation a single maximum of the scattered intensity is observed in the center of the scan range, when the silicon particle is in contact with the silver particle. In *s*-polarisation two maxima appear, shifted along the *y* axis, i.e. in the direction of the electric field. The qualitative features of the image obtained in *s*-polarisation can be explained as follows. Along the *x* axis at $y = 0$ the incidence is always in-plane with the pair axis of the probe–sample pair. Then, only the transverse mode is excited. For all other *y* positions, the incidence is out of plane with the pair axis and the electric field vector can be decomposed into two components parallel and perpendicular to the pair axis. Then, the more efficient longitudinal mode is also excited to a certain amount. Hence the scattered intensity increases and approaches maxima close to $x = \pm 35$ nm but in direction of the incident electric field. In *p*-polarisation the scattered intensity is always dominated by the longitudinal mode and becomes maximum at $x = 0$ and $y = 0$ where only the longitudinal mode contributes to the intensity pattern. At large distances of the probe cluster the intensity tends to a constant value which is the sum of the intensities scattered by the isolated silicon and silver cluster. This value is different in *s*- and *p*-polarisation as the scattering of evanescent waves by single clusters is polarisation-dependent.

In Fig. 5 we show the dependence of the scattered intensities on the height *z* of the probe particle for the same clusters as in Fig. 4. For that purpose the scans were performed only at $y = 0$ along the *x* axis with *z* varying from $z = 50$ nm (touching spheres) to $z = 75$ nm for the center of the silicon particle relative to the glass substrate in steps of $\delta z = 5$ nm. In *p*-polarisation the maximum at $x = 0$ and $y = 0$ obviously decreases with increasing height. For still larger heights it can be expected that finally the intensity is everywhere the same as the intensity of two well-separated

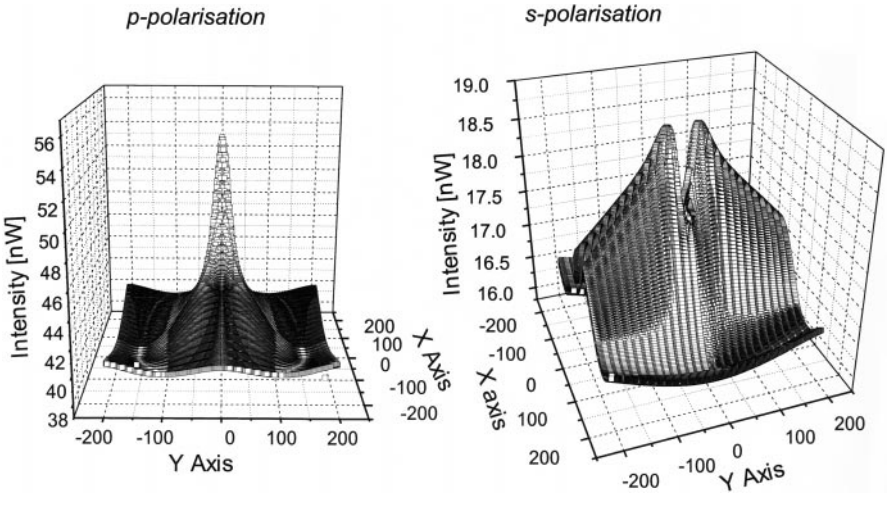

Fig. 4. Three-dimensional plot of the scattered intensity in *p*- and *s*-polarisation of an incident evanescent wave for the scan of a Si-cluster ($2a_0 = 20$ nm) across a surface with a single spherical Ag-cluster ($2a_1 = 40$ nm)

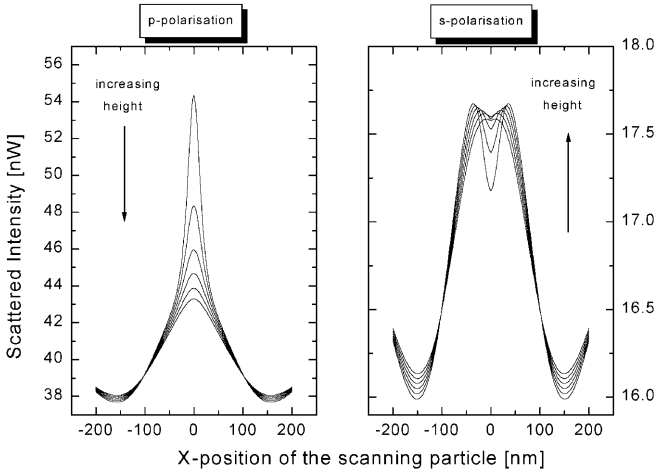

Fig. 5. Two-dimensional plot at $y = 0$ of the scattered intensity in *p*- and *s*-polarisation of an incident evanescent wave for the scan of a Si-cluster ($2a_0 = 20$ nm) across a surface with a single spherical Ag-cluster ($2a_1 = 40$ nm). The height z of the scanning particle is varied from $z = 50$ nm (touching spheres at $x = 0$, $y = 0$) to $z = 75$ nm in steps of $\delta z = 5$ nm

clusters. In *s*-polarisation the results are similar, except that at $x = 0$ and $y = 0$ the intensity has a minimum and two maxima at about $x = \pm 35$ nm. As these maxima shift towards $x = 0$ with increasing height of the scanning probe cluster, the minimum becomes less deep with increasing height and finally vanishes for sufficiently large heights. It is worth mentioning that these intensity patterns are different from that obtained for plane waves in grazing incidence, due to the complex phase shift of the evanescent wave. Exemplary intensity patterns for plane waves are shown in a previous paper [23].

In many further calculations we examined the dependence of these results on particle sizes, particle materials and the wavelength of the incident wave. The results are summarized in the following.

2.1 Particle sizes

The probe cluster size was varied between 10 nm and 20 nm in diameter. The sample cluster size was varied between 10 nm and 60 nm in diameter. In dependence on the particle sizes the total scattered intensity increases with increasing size. However, the basic features of the previous scans remain almost unchanged. An example is given in Fig. 6 for a silicon particle with $2a_0 = 20$ nm and for a silver particle with the size varying between $2a_1 = 10$ nm and $2a_1 = 60$ nm. In *p*-polarisation the width of the maximum depends on the cluster size. Also in *s*-polarisation a size dependence can be seen but is not so obvious as in *p*-polarisation.

2.2 Particle materials

For the probe material Si and Si_3N_4 were used, which are commonly used materials in near-field microscopy. For the sample material we used Ag, GaAs, and SiO_2 representatively for metals, semiconductors, and isolators. Again, the basic features of the previous scans remain almost unchanged, however, the total intensity depends on the material.

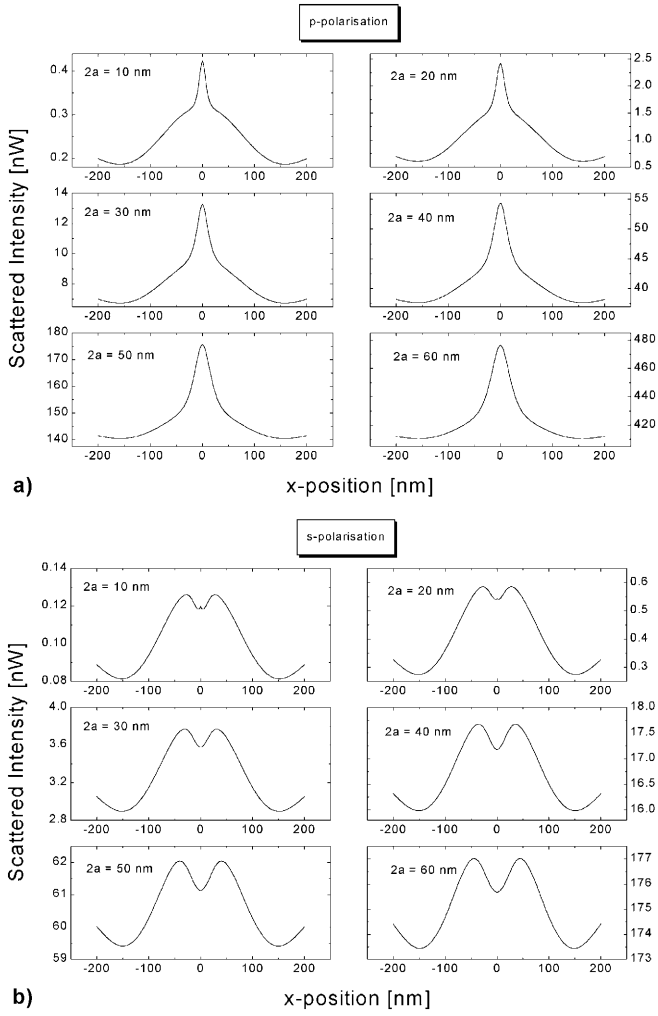

Fig. 6. Two-dimensional plot at $y = 0$ of the scattered intensity in *p*- and *s*-polarisation of an incident evanescent wave for the scan of a Si-cluster ($2a_0 = 20$ nm) across a surface with a single spherical Ag-cluster of varying particle size. The size of the Ag-cluster is varied from $2a_1 = 10$ nm to $2a_1 = 60$ nm in steps of $\delta(2a_1) = 10$ nm

In *s*-polarisation the minimum at $x = 0$ has already vanished for the cluster pairs Si−GaAs and Si−SiO_2 and is replaced by a narrow maximum. The material dependence of the scattered intensity results from the different optical constants and is similar to the material dependence of the scattering by single particles. For demonstration consider the scattering cross section of a single cluster that is very small compared to the wavelength of the incident light (Rayleigh approximation). In this limit the scattering cross section is

$$\sigma_{\mathrm{sca}} = \frac{128\pi^5 n_{\mathrm{M}}^4}{9}\frac{a^6}{\lambda^4}\left|\frac{\varepsilon - \varepsilon_{\mathrm{M}}}{\varepsilon + 2\varepsilon_{\mathrm{M}}}\right|^2 . \qquad (8)$$

For particles of equal size and at constant wavelength λ the cross section differs only by the dielectric constants ε of the particle material and ε_{M} of the surrounding medium (here: air). The dielectric constants of various materials and the resulting cross sections for particles with $2a = 20$ nm at wavelength $\lambda = 514$ nm are summarized in Table 1.

It becomes obvious that the silver particle has the largest cross section followed by silicon, GaAs, Si_3N_4, and silica.

Table 1. Values for the dielectric constant and the scattering cross section of very small particles in the Rayleigh limit of same size and at the same wavelength $\lambda = 514\,\text{nm}$

Material	Dielectric constant ε	$\sigma_{\text{sca}} \propto \left\lvert \frac{\varepsilon-\varepsilon_{\text{M}}}{\varepsilon+2\varepsilon_{\text{M}}} \right\rvert^2$
Ag	$-10.3+i\cdot 0.205$	1.853
GaAs	$17.66+i\cdot 3.207$	0.725
Si	$17.89+i\cdot 0.525$	0.72
Si_3N_4	$4.15+i\cdot 0$	0.263
SiO_2	$2.13+i\cdot 0$	0.075

From further calculations we found, however, that in scans with a Si_3N_4 probe across a surface with clusters the scattered intensity is almost the same as in scans of silicon probe. Hence, for near-field microscopy, it seems appropriate to use also Si_3N_4 instead of Si for the probe.

2.3 Wavelength

For comparison of the scattered intensity at different wavelengths we calculated scans of a Si-probe ($2a_0 = 20\,\text{nm}$) over a surface with a silver cluster ($2a_1 = 40\,\text{nm}$) at wavelengths $\lambda_1 = 514\,\text{nm}$ and $\lambda_2 = 633\,\text{nm}$, which are the most-used laser wavelengths in common scattering experiments. The results are not shown here but are discussed in the following. The ratio $I(\lambda_1)/I(\lambda_2)$ approximately amounts to 2.94 for *p*-polarisation and 2.83 for *s*-polarisation. These ratios are close to the ratio $(\lambda_1/\lambda_2)^4 = 2.3$ that is expected from single-particle scattering in the Rayleigh limit. The difference is caused by the electromagnetic coupling among the clusters that already in the Rayleigh limit affects scattering and absorption [22].

3 Results and discussion for aggregates of clusters on a substrate

In this section we turn to exemplary results for aggregates of clusters. Without any restriction of the generality of the results the clusters in the aggregates were assumed to be identical in size and material. These assumptions strongly reduce the manifold of parameters that must be taken into account in this scattering problem. For further reduction we restrict ourselves to the discussion of *x*-*y*-*z* scans in *p*-polarisation of the incident evanescent wave. It is a preliminary result and an obvious conclusion drawn from the scans presented in the preceding section that for the purpose of imaging nanostructures by means of apertureless optical near-field microscopy employing total internal reflection it is preferable to use *p*-polarised excitation. Nevertheless, for all aggregates discussed in the following, also intensities in *s*-polarisation were calculated, but will not presented in this paper. The geometry of the exemplary aggregates is sketched in Fig. 7. Aggregate 1 is a linear chain of $N = 5$ identical Ag particles with $2a_1 = 40\,\text{nm}$. Aggregate 2 and aggregate 3 are identical in their topology, but for aggregate 2 all particles are in the *x*-*y* plane whereas for aggregate 3 the fifth particle is centered at $z = 60\,\text{nm}$ above the fourth cluster. Hence, it seems appropriate to make line scans at different *y* positions for aggregate 2 whereas for aggregate 3 line scans at different heights of the silicon particle will be of greater interest. In all scans the size

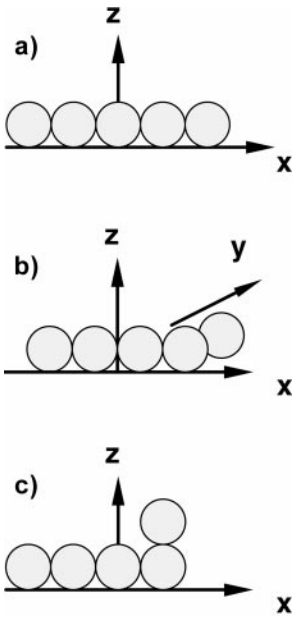

Fig. 7a–c. Sketch of the aggregates of $N = 5$ identical Ag-clusters ($2a_1 = 40\,\text{nm}$). **a** Aggregate 1 (linear chain of spheres). **b** Aggregate 2. **c** Aggregate 3

of the scanning silicon particle is $2a_0 = 20\,\text{nm}$. The wavelength is $\lambda = 514\,\text{nm}$.

Starting with the linear chain (aggregate 1), Fig. 8 depicts the line scans along the *x* axis at $y = 0$ (Fig. 8a) and $y = \pm 40\,\text{nm}$ (Fig. 8b) and the height $z = 50\,\text{nm}$. Obviously, the scans at $\pm 40\,\text{nm}$ are identical, indicating a symmetry along the *y* axis. Along the *x* axis all scans are slightly asymmetric when going from $-x$ to x. The asymmetry is caused by retardation in the excitation of the particles in the chain: the evanescent wave is phase shifted at each particle site when propagating along the *x* axis. In Fig. 8a six intensity maxima with five intensity minima in between can clearly be resolved. The number of minima corresponds to the number of particles in the chain, whereas the number of maxima is increased by 1. This result was also obtained in further line scans along linear chains with varying number *N* of clusters, as long as the

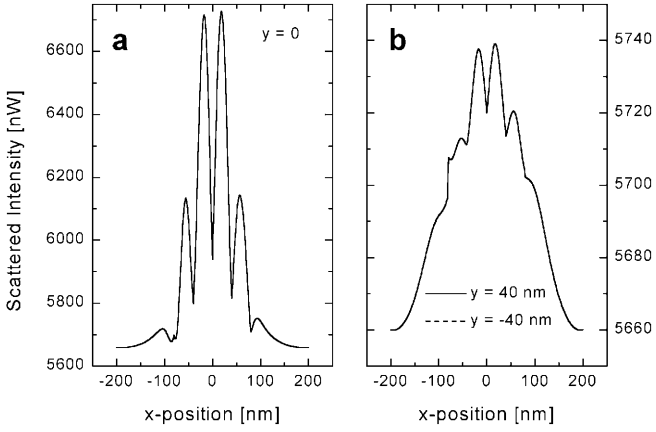

Fig. 8a,b. Two-dimensional plot of the scattered intensity in *p*- and *s*-polarisation of an incident evanescent wave for the scan of a Si-cluster ($2a_0 = 20\,\text{nm}$) across a surface with aggregate 1 at $y = 0$ (**a**), at $y = \pm 40\,\text{nm}$ (**b**). The height *z* amounts to $z = 50\,\text{nm}$

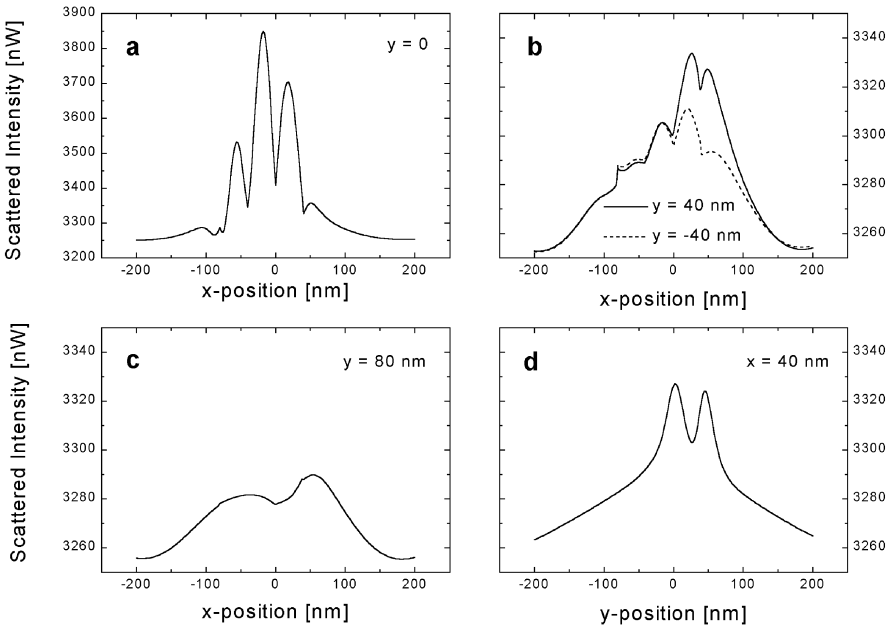

Fig. 9a–d. Two-dimensional plot of the scattered intensity in *p*- and *s*-polarisation of an incident evanescent wave for the scan of a Si-cluster ($2a_0 = 20$ nm) across a surface with aggregate 2 at $y = 0$ (**a**), at $y = \pm 40$ nm (**b**), at $y = 80$ nm (**c**), along the y axis at $x = 40$ nm (**d**). The height z amounts to $z = 50$ nm

number N is below $N = 8$. For larger N the influence of further particles in the chain decreases with increasing N, resulting in deviations from the above rule. This dependence on N also affects extinction and scattering spectra and was already discussed in [25]. The distance of the peak positions of the outermost maxima $\delta x = 196$ nm approximately corresponds to the length of the aggregate in x direction (200 nm), although the positions of these maxima are slightly shifted compared to the physical ends of the aggregate. This result was not confirmed by further calculations on linear chains with varying N. For example, for a linear chain of $N = 2$ spheres with $2a = 40$ nm the distance of the outermost peak positions amounts to $\delta x = 56$ nm instead of 80 nm, for a linear chain with $N = 6$ spheres it amounts to $\delta x = 250$ nm instead of 240 nm.

In the line scans at $y = \pm 40$ nm (Fig. 8b) the intensity is strongly reduced due to the larger distance of the scanning probe from the aggregate. However, the features of Fig. 8a are kept except that the minima are less resolved than in Fig. 8a.

For aggregate 2 intensity curves from line scans along the x axis at $y = 0$, ± 40 nm and 80 nm and a line scan along the y axis at $x = 40$ nm are shown in Fig. 9. Comparing first the line scan at $y = 0$ (Fig. 9a) with the corresponding line scan for the linear chain in Fig. 8a, some similarities can be recognized. However, now the intensity is reduced by approximately a factor 1.8. Furthermore, only five maxima with four minima in between can be resolved. Hence, the aggregate 2 appears to be a linear chain of $N = 4$ particles. In contrast, the intensity pattern is asymmetric in the sense that the fourth and fifth maximum are increased. This is caused by the coupling with the fifth particle which is aside the fourth particle in the chain (see Fig. 7b).

The influence of this particle can also clearly be recognized in the line scans at $y = -40$ nm, 40 nm, and 80 nm in Fig. 9b and c. At $y = -40$ nm the coupling of the probe cluster with this particle is the smallest, hence, the line scan is dominated by the four particles in the chain. At $y = 40$ nm the interaction becomes the strongest. Therefore, the fourth and fifth maximum becomes approximately of equal magnitude. Finally, at $y = 80$ nm the coupling among the probe and the sample is dominated by the coupling with particles 4 and 5. Then, only a broad intensity peak at approximately $x = 60$ nm remains in the intensity pattern (Fig. 9c).

Figure 9d shows in addition the line scan at $x = 40$ nm along the y axis. In this scan direction the probe mainly interacts with particles 3, 4, and 5. The scan exhibits 2 maxima with 1 minimum in between and is asymmetric due to the different influence of the various particles in the aggregate.

The discussion of the intensity pattern obtained for aggregate 3 is different from that of aggregates 1 and 2 because the probe particle must scan across the surface at different heights. Starting with the line scans at $y = \pm 40$ nm which were done at $z = 50$ nm, it becomes obvious from Fig. 10b that they are identical. The features are similar to those of aggregate 2 in Fig. 9b. However, the first maximum at about $x = -100$ nm is not resolved as well as the minimum between first and second maximum. As the fifth particle is now

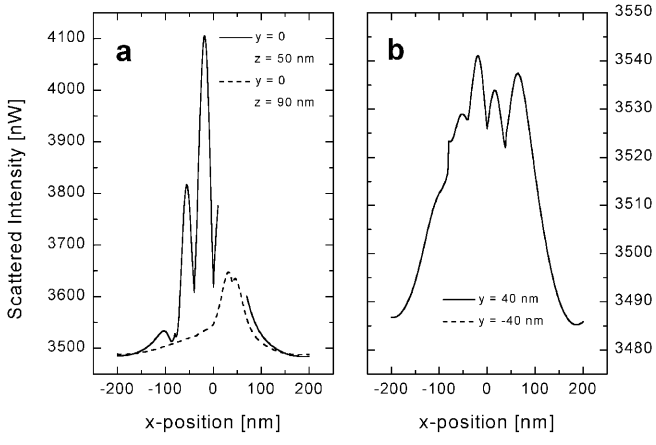

Fig. 10a,b. Two-dimensional plot of the scattered intensity in *p*- and *s*-polarisation of an incident evanescent wave for the scan of a Si-cluster ($2a_0 = 20$ nm) across a surface with aggregate 3 at $y = 0$ for two heights $z = 50$ nm and $z = 90$ nm (**a**), at $y = \pm 40$ nm and height to $z = 50$ nm (**b**)

centered at $x = 40$ nm and $z = 60$ nm, i.e. above the fourth particle, its influence on the intensity pattern is different from that for aggregate 2. In particular, the magnitudes of the fourth and fifth maximum have turned: now the magnitude of the fifth maximum is larger than the magnitude of the fourth maximum. In turning to the discussion of the line scan at $y = 0$ in Fig. 10a, two intensity curves are plotted. The first curve for $z = 50$ nm is incomplete because at this height the scanning probe cluster hits the fifth particle at $x = 20$ nm and cannot be further moved along the x axis without lifting. Continuation of the scan at this height is possible again at $x = 60$ nm. Between $x = 20$ nm and $x = 60$ nm the probe must be lifted so that its center is minimum at $z = 90$ nm. The resulting intensity curve at this new height is shown for the whole scan region as the dashed line in Fig. 10a. It is evident that in this case the main contribution comes from the electromagnetic interaction among the probe cluster and the clusters 4 and 5 in the aggregate.

4 Summary

In this paper we extended evanescent wave scattering on scattering by aggregates of particles or clusters. This increasingly becomes important in the field of scanning optical near-field microscopy employing evanescent waves from total internal reflection on a transparent plane surface, because in these applications the nanostructures may be replaced by an aggregate of spherical particles with different sizes. In this paper we have restricted ourselves to exemplary aggregates with identical clusters. Further discussion is necessary for aggregates with particles of different sizes, which will be done in a forthcoming paper.

After a brief introduction to the basics of the underlying theory we started with *x*-*y*-*z* scans of a near-field probe across a surface with single clusters. For that purpose the probe was replaced by a single cluster. The scans were performed at different heights z of the scanning probe across a surface with the single cluster in the center of the *x*-*y* plane. We varied the sizes of probe and sample, and studied the influence of the cluster materials on the scans, and the wavelength was also varied. In all scans the main features in the scattered intensity – a maximum intensity at $x = 0$, $y = 0$ in *p*-polarisation, and a minimum intensity at $x = 0$, $y = 0$ in *s*-polarisation – were independent of the cluster sizes and materials and independent of the wavelength. The magnitude of the scattered intensity, however, clearly depends on these parameters, and it can be concluded that the scattering is the strongest for metallic clusters. The intensity increases with increasing cluster size and decreases with increasing wavelength. A further conclusion of these scans is that for the purpose of imaging nanoparticles by means of apertureless near-field optical microscopy in a setup employing TIR it is preferable to use *p*-polarised excitation.

Hence, the *x*-*y*-*z* scans across a surface with aggregates of clusters were restricted to *p*-polarisation of the incident evanescent wave. When scanning across an aggregate the scattered intensity shows maxima and minima. We found as a general rule that the number of maxima is $N + 1$ and the number of minima is N, when N is the number of identical particles in the aggregate along the scan direction. This result holds true as long as $N \leq 8$. The distance between the outermost maxima in general does not agree with the total length of the aggregate in scan direction. The determination of heights is more difficult and requires further numerical studies. This is also of interest because in a real experiment, it is usually not the total scattered intensity that is being measured, but rather the oscillating component of the scattered intensity, while the probe is dithered in the z direction. In this case, background signal is suppressed. This will also be discussed in a forthcoming paper.

In conclusion the calculations showed that evanescent light scattering is a useful method to obtain images of a scattering subject. However, the evaluation of the intensity pattern according to size and shape of the scattering subject is determined by the scattering of the evanescent wave also by the probe and the electromagnetic interaction among probe and sample. The latter smoothes the sharp geometrical contures of the sample and yields minima and maxima in the scattered intensity which cannot directly be attributed to the topology of the sample. Hence, further discussion of the intensity pattern is necessary to obtain information about size and shape of the sample. Basing upon the presented results, in forthcoming numerical studies an algorithm will be developed that allows correction of the intensity pattern for the effects of electromagnetic coupling.

References

1. R.C. Reddick, R.J. Warmack, T.L. Ferrell: Phys. Rev. B **39**, 767 (1989)
2. R.C. Reddick, R.J. Warmack, D.W. Chilcott, S.L. Sharp, T.L. Ferrell: Rev. Sci. Instrum. **61**, 3669 (1990)
3. F. Zenhausern, Y. Martin, H.K. Wickramasinghe: Science **269**, 1083 (1995)
4. Y. Martin, F. Zenhausern, H.K. Wickramasinghe: Appl. Phys. Lett. **68**, 2475 (1996)
5. H. Chew, D.S. Wang, M. Kerker: Appl. Opt. **18**, 2679 (1979)
6. C. Liu, T. Kaiser, S. Lange, G. Schweiger: Opt. Commun. **117**, 521 (1995)
7. M. Quinten, A. Pack, R. Wannemacher: Appl. Phys. B **68**, 87 (1998)
8. R. Wannemacher, A. Pack, M. Quinten: Appl. Phys. B **68**, 225 (1998)
9. C. Hafner: *The Generalized Multipole Technique for Computational Electromagnetics* (Artech House Books 1990)
10. B. Labani, C. Girard, D. Courjon, D. Van Labeke: J. Opt. Soc. Am. B **7**, 936 (1990)
11. C. Girard: Appl. Opt. **31**, 5380 (1992)
12. C. Girard, A. Dereux: Phys. Rev. B **49**, 11344 (1994)
13. L. Novotny: J. Opt. Soc. Am. A **14**, 105 (1997), and references 2–8 therein
14. M. Xiao: J. Opt. Soc. Am. A **14**, 2977 (1997)
15. M. Quinten, U. Kreibig, D. Schönauer, L. Genzel: Surf. Sci. **156**, 741 (1985)
16. U. Kreibig, D. Schönauer, M. Quinten: Phys. Scr. **T13**, 84 (1986)
17. M. Quinten, U. Kreibig: In *Optical Particle Sizing*, ed. by G. Gouesbet, G. Gréhan (Plenum press, New York 1988) pp. 249–258
18. M. Quinten, D. Schönauer, U. Kreibig: Z. Phys. **D12**, 521 (1989)
19. D. Schönauer, M. Quinten, U. Kreibig: Z. Phys. **D12**, 527 (1989)
20. U. Kreibig, K. Fauth, D. Schönauer, M. Quinten: Z. Phys. **D12**, 505 (1989)
21. T. Kahlau, M. Quinten, U. Kreibig: Appl. Phys. A **62**, 19 (1996)
22. M. Quinten: *Physical and Chemical Properties of Surfaces in Nano-Particle Systems*, Aachener Beiträge zur Physik kondensierter Materie, Vol. 24 (Wissenschaftsverlag Mainz, Aachen 1998)
23. M. Quinten: Appl. Phys. B **67**, 101 (1998)
24. C.F. Bohren, D.R. Huffman: *Absorption and Scattering of Light by Small Particles* (Wiley, New York 1983)
25. M. Quinten, U. Kreibig: Appl. Opt. **32**, 6173 (1993)